Physics of Fluids

Shrinkage induced flow during directional solidification of pure substance in a bottom cooled cavity: A study on flow reversal phenomena

Cite as: Phys. Fluids **32**, 047104 (2020); https://doi.org/10.1063/5.0002953
Submitted: 29 January 2020 . Accepted: 27 March 2020 . Published Online: 14 April 2020

Aniket D. Monde, Oaj Chawla, Virkeshwar Kumar, Shyamprasad Karagadde, and Prodyut R. Chakraborty

Shrinkage induced flow during directional solidification of pure substance in a bottom cooled cavity: A study on flow reversal phenomena

Cite as: Phys. Fluids 32, 047104 (2020); doi: 10.1063/5.0002953
Submitted: 29 January 2020 • Accepted: 27 March 2020 •
Published Online: 14 April 2020

Aniket D. Monde,[1] Oaj Chawla,[1] Virkeshwar Kumar,[2] Shyamprasad Karagadde,[2] and Prodyut R. Chakraborty[1,a)]

AFFILIATIONS

[1] Department of Mechanical Engineering, Indian Institute of Technology Jodhpur, Jodhpur 342037, India
[2] Department of Mechanical Engineering, Indian Institute of Technology Bombay, Mumbai 400076, India

[a)] **Author to whom correspondence should be addressed:** pchakraborty@iitj.ac.in

ABSTRACT

Development and proposition of a numerical model to capture the shrinkage induced flow during directional solidification of a pure substance in a bottom cooled cavity are carried out. A novel numerical scheme involving fixed grid-based volume fraction updating is proposed to track the solid–liquid interface, considering the inclusion of the shrinkage effect. Directional solidification in bottom cooled orientation is of particular interest since shrinkage and buoyancy effects oppose each other. The results from the proposed numerical model indicated the existence of an unprecedented flow reversal phenomenon during the progression of the solidification process, caused by the opposing nature of shrinkage and buoyancy effects. The flow reversal phenomena predicted by the numerical model are validated by conducting experiments involving directional solidification of coconut oil in a bottom cooled cavity. Qualitative and quantitative measurements of the velocity field and interface growth are obtained using the particle image velocimetry technique and compared with three dimensional numerical results. Once the flow reversal phenomena are established through numerical and experimental evidences, case studies are performed, considering varying material properties, cold boundary temperatures, initial temperatures of the melt, and cavity heights to find the effect of each of these parameters on flow reversal phenomena. The parametric study also allowed us to check the robustness and consistency of the proposed model. The proposed model will serve as an important milestone toward the development of numerical models for capturing macro-scale shrinkage defects and prediction of composition heterogeneity during directional alloy solidification.

NOMENCLATURE

Variables

c_p	specific heat (J/kg K)
f	mass fraction
g	volume fraction
g_a	gravitational acceleration (m/s^2)
H	height (mm)
h	enthalpy (J/kg)
h_{sl}	latent heat (J/kg)
k	thermal conductivity (W/mK)
p	pressure (Pa)
T	temperature (K)
T_b	cold boundary temperature (K)
T_L	liquidus temperature (K)
T_m	melting temperature (K)
T_S	solidus temperature (K)
u, v, w	magnitude of velocity in x, y, and z directions, respectively (mm/s)
$\vec{\mathbf{V}}$	velocity vector (m/s)
W	width (mm)
x, y, z	coordinate axes

Greek symbols

β	volume expansion coefficient (K^{-1})
ε	constant
ρ	density (kg/m^3)
μ	viscosity (kg/ms)

Subscripts

C	cavity
i	initial
int	interface
l	liquid
ref	reference value
R	riser
s	solid

I. INTRODUCTION

Phase change processes associated with solidification and melting are an intrinsic component of manufacturing processes, such as casting and welding, and thermal management applications involving latent heat thermal energy storage and cyclic cooling of electronic equipment. The physics associated with the solidification process is multi-scale in nature, spanning from nano- to macro-scale. State-of-the-art manufacturing technologies such as additive manufacturing processes involving laser sintering and laser surface alloying essentially deal with melting and re-solidification mechanisms. Numerous complex flow physics involving Marangoni convection due to surface tension,[1–4] natural convection, and shrinkage convection[5–7] play a key role in defining the desirable mechanical properties of the products manufactured through such advanced processes. Thus, the understanding of such flow physics is of utmost importance to obtain an improved product yield from these processes. The broad area of primitive, contemporary, and advanced manufacturing applications pertinent to the melting and solidification process instigated commendable research outcomes by several research groups over the past few decades.

Regardless of clarity in definition, the issues associated with the solidification are complex to perceive. The foremost concern related to the solidification phenomenon is to track the evolving solid–liquid interface. There exists three classes of solidification processes, namely, (a) distinct, (b) alloy, and (c) continuous. The distinct solidification process involves the existence of a sharp interface between solid and liquid phases, typically featuring solidification of pure metals. The alloy solidification process involves regions of columnar and equi-axed crystalline structures with complex shapes of the solid–liquid interface, typically encountered during solidification of metal alloys. For the continuous solidification process, the individual phases are dispersed in every part of the phase change region and no distinct interface exists. Typical examples of the continuous solidification process are freezing of oil, wax, and polymers. Distinct interface tracking can be achieved by the well-established front tracking method,[8–10] level set method,[11] and marker and cell method.[12] However, for alloy and continuous solidification processes, the interface is hardly distinct, and the tracking methods are computationally expensive and difficult to implement.[13] One of the reliable schemes to address all three types of solidification processes is the fixed grid based enthalpy or volume fraction updating method. The major advantage of the fixed grid enthalpy updating method[13] is the redundancy of explicit coupling requirements for energy and mass balance at the interface location. A considerable number of numerical models involving the well-established enthalpy updating scheme to solve pure metal or binary alloy solidification have been reported by several researchers.[14–19]

The enthalpy updating formulation for capturing the solid–liquid interface during solidification of pure metals and binary alloys was originally proposed by Voller *et al.*[14,15] The key features of the formulation proposed by Voller *et al.*[14,15] are the inclusion of local variation of latent heat of fusion as a source term in the energy conservation equation and the iterative evolution of the same. Brent *et al.*[16] proposed a further modification of the model originally proposed by Voller *et al.*[14,15] and reported that a faster convergence is possibly obtained for the solidification under the effect of natural convection by using an enthalpy porosity approach. Recently, Chakraborty[19] proposed a modified enthalpy updating method that evaluates the solid or liquid volume fraction and simulates the phase change process of materials with substantial variation between phase specific heats.

All the enthalpy updating based solidification models proposed until date have the limitation of considering the same density of liquid and solid phases. Shrinkage or volumetric expansion effects due to the difference of liquid and solid phases is an important aspect of the solidification process for most of the pure substances and alloys. The incorporation of the effects of different phase densities within the present framework of the enthalpy updating scheme will lead to a more reliable numerical scheme to predict the evolution of all three types of solidification processes. Existing solidification models involving the shrinkage effect are rarely found.[20–23] Among the few existing models involving the shrinkage effect, the pioneering model was proposed by Chiang and Tsai.[21,22] The analysis reported by Chiang and Tsai[21,22] involves directional solidification from the bottom side of 1% Cr–steel in a rectangular cavity with a riser at the center. This particular configuration was chosen to suppress all other possibilities of natural convection due to side[24] and top cooling,[25] while the shrinkage induced flow takes the lead role in shaping the solid front growth. However, the absence of the source term associated with natural convection in the analysis reported by Chiang and Tsai[21] nullified any possibility of interaction between the buoyancy and shrinkage induced source terms from the modeling point of view. The possibility of such interaction needs to be explored further. The study of shrinkage induced convection is particularly crucial, since convection in the liquid and mushy regions plays a key role in enhancing or suppressing casting defects such as macro-segregation, porosity, and hot tears.[26] Experiments involving directional solidification in the bottom cooled configuration are performed to study macro-segregation,[27–30] grain growth of metals and their alloys,[31–33] and convection owing to the density anomaly of fluid.[34–36] To the best knowledge of the present authors, no experimental study addressed the shrinkage induced flow and its effect on solid front growth until date.

Based on the existing literature survey, the following objectives are postulated and studied: (a) improvement of the existing enthalpy updating scheme by incorporating the shrinkage effect, (b) investigation of the shrinkage induced flow and its effect on solid front growth during the continuous and distinct solidification processes,

(c) investigation on the interaction between the shrinkage induced source term and the buoyancy source term, (d) exploring the possibility of implementing the pressure boundary condition within the Semi-Implicit Method for Pressure-Linked Equations Revised (SIMPLER) algorithm frame work,[37] and (e) quantitative and qualitative validation of the proposed model with the experimental findings. The presented numerical model is limited to predict the effect of the shrinkage induced flow on solid front growth during distinct and continuous directional solidification processes associated with pure metals, oils, wax, and other polymeric substances, not alloys. However, evolution of the mushy zone is accounted for, since oils, wax, and other polymeric substances freezes over a fixed temperature range. Hence, upgradation of the proposed model for predicting alloy solidification is expected to be attainable and left as the future scope. For two dimensional (2D) numerical analysis, solidification of pure aluminum (Al) and copper (Cu) is studied, whereas for 3D numerical and experimental investigations, solidification of coconut oil is studied.

II. MATHEMATICAL MODELLING

The physical domain for which the numerical and experimental investigations are performed is shown in Fig. 1. The physical domain is set in a similar fashion, as reported by Chiang and Tsai,[21] to address the effect of the shrinkage induced flow during directional solidification from the bottom surface. The domain consists of a rectangular cavity with a riser at the center (Fig. 1). The cavity is initially filled with a liquid material above the freezing temperature range ($T_i > T_L$). Solidification ensues as the temperature of the bottom wall is set below the solidus temperature (T_S). All other sides of the cavity are insulated. It is assumed that the riser is continuously fed with the liquid melt from a source tank located above the riser.

The volume averaged continuum formulation of mass and momentum balance originally proposed by Bennon and Incropera[38]

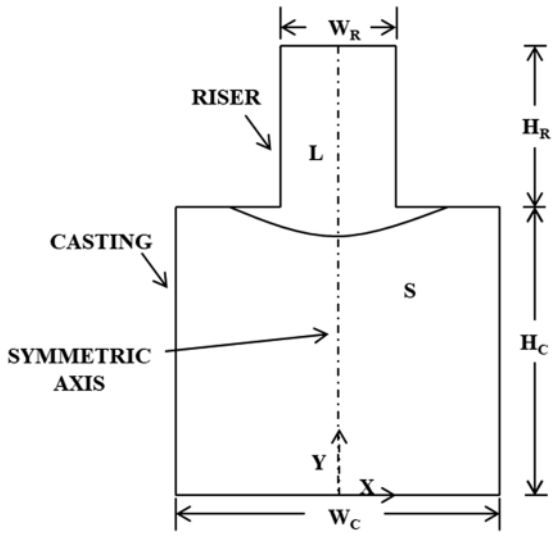

FIG. 1. Schematic of the physical domain of interest.

and later modified by Chiang and Tsai[21] to incorporate the shrinkage effect has been used for the present numerical model. The volume fractions of liquid and solid phases are defined as g_l and g_s, respectively, while the liquid and solid mass fractions are estimated to be $f_l = g_l\rho_l/\rho$ and $f_s = g_s\rho_s/\rho$, respectively. For both volume and mass fractions, $g_l + g_s = 1$ and $f_l + f_s = 1$, respectively. It is assumed that thermo-physical properties are different for liquid and solid phases. However, for individual phases, these properties do not vary with temperature. As the shrinkage effect is considered, liquid and solid phases have different densities ($\rho_s \neq \rho_l$). Defining the volume averaged density as $\rho = g_l\rho_l + g_s\rho_s$ and the mass averaged velocity as $\vec{V} = f_l\vec{V}_l + f_s\vec{V}_s = (g_l\rho_l/\rho)\vec{V}_l + (g_s\rho_s/\rho)\vec{V}_s$, the conservation equations for mass and momentum are given as follows:

continuity

$$\frac{\partial}{\partial t}(\rho) + \nabla\cdot\left(\rho\vec{\mathbf{V}}\right) = 0, \tag{1}$$

momentum

$$\frac{\partial}{\partial t}(\rho u) + \nabla\cdot\left(\rho\vec{\mathbf{V}}u\right) = \nabla\cdot\left(\mu_l\frac{\rho}{\rho_l}\nabla u\right) - \frac{\partial p}{\partial x} - \frac{\mu_l}{K}\frac{\rho}{\rho_l}u - \nabla\cdot\left(\rho\frac{g_s\rho_s}{g_l\rho_l}\vec{\mathbf{V}}u\right) + \nabla\cdot\left(\mu_l u\nabla\left(\frac{\rho}{\rho_l}\right)\right), \tag{2}$$

$$\frac{\partial}{\partial t}(\rho v) + \nabla\cdot\left(\rho\vec{\mathbf{V}}v\right) = \nabla\cdot\left(\mu_l\frac{\rho}{\rho_l}\nabla v\right) - \frac{\partial p}{\partial y} - \frac{\mu_l}{K}\frac{\rho}{\rho_l}v - \nabla\cdot\left(\rho\frac{g_s\rho_s}{g_l\rho_l}\vec{\mathbf{V}}v\right) + \nabla\cdot\left(\mu_l v\nabla\left(\frac{\rho}{\rho_l}\right)\right) + \rho^l_{ref}g_a\beta\left(T - T_{ref}\right). \tag{3}$$

The fifth term appearing on the right-hand side of u and v momentum conservation equations (2) and (3) represent the source term associated with the shrinkage effect. This particular source term solely accounts for the shrinkage induced fluid flow during the solidification process. The fourth term appearing on the right-hand side of Eqs. (2) and (3) represent inertial forces within the mushy region where the liquid volume fraction varies within the range of $0 < g_l < 1$. The third term on the right-hand side of Eqs. (2) and (3) represents the Darcian damping force term for the porous medium, once again of relevance only within the mushy region. The effect of the inertia terms is typically found to be negligible, as compared to the Darcian damping term.[21,38] However, for the sake of generality, the inertia term has been retained for the present model. K appearing in the Darcian damping force source terms is defined as follows:[39]

$$K = K_0\left(\frac{g_l^3 + \varepsilon}{(1 - g_l)^2}\right), \tag{4}$$

where ε is a very small number ($\sim 10^{-8}$) to restrain the Darcian term from blowing off numerically as $g_l \to 0$ and K_0 is the permeability constant. The last term appearing on the right-hand side of v-momentum equation (3) represents the natural convection or buoyancy term in the liquid melt, where ρ^l_{ref}, g_a, and β are the reference melt density, gravitation, and volume expansion coefficient of the melt, respectively. It is important to mention here that Chiang and Tsai[21] excluded the buoyancy source term from their analysis during the bottom cooled configuration, thereby nullifying any

chance of interaction between the shrinkage induced source term and the buoyancy source term. They,[22] however, included the buoyancy source term for the side cooling case study. The conservation equations are formulated on the assumption that the phase velocity within the solid remains immobile, i.e., $\vec{V}_s = 0$.

The energy conservation equation is again derived on the basis of the volume averaged continuum formulation originally proposed by Bennon and Incropera.[38] Mass averaged enthalpy is defined as $h = f_l h_l + f_s h_s$, where h_s and h_l are the respective phase enthalpies in solid and liquid defined as $h_s = c_{ps}T$ and $h_l = (c_{ps} - c_{pl})T_S + h_{sl} + c_{pl}T$, respectively. c_{ps} and c_{pl} are specific heat capacities for solid and liquid phases, respectively. T_S is the solidus temperature of the amorphous substance. The energy equation is expressed in terms of temperature as the scalar variable, rather than the volume averaged enthalpy.[19] The latent heat appears in conjunction with the liquid volume fraction in one out of the three source terms of the energy conservation equation (5). The fourth term appearing on the right-hand side of the energy conservation equation (5) also contains the liquid volume fraction. It is to be noted that two out of the three source terms (second and fourth term) in the energy conservation equation (5) appear if there exists a difference between liquid and solid specific heats, and both of these source terms vanish when liquid and solid phases have the same specific heat capacity, i.e., $c_{ps} = c_{pl}$. A volume fraction updating method is employed to estimate the solid/liquid volume fraction over the entire domain to capture solid, mushy (containing dispersed solid and liquid phases), and liquid regions. The mushy region is defined by a temperature range within liquidus (T_L) and solidus (T_S) (upper and lower limits of the freezing temperature range) temperatures, respectively. The conservation of energy is given as follows:[19]

energy

$$\frac{\partial}{\partial t}(\rho T) + \nabla \cdot \left(\rho \vec{\mathbf{V}} T\right) = \nabla \cdot \left(\frac{k}{c_{ps}} \nabla T\right) - \nabla \cdot \left[\left(\frac{c_{pl}}{c_{ps}} - 1\right)\rho \vec{\mathbf{V}} T\right] - \frac{\partial}{\partial t}\left(\frac{\rho_s g_l h_{sl}}{c_{ps}}\right) - \frac{\partial}{\partial t}\left[g_l \left(\frac{c_{pl}}{c_{ps}} - 1\right)(\rho_l T - \rho_s T_S)\right]. \quad (5)$$

Since the solidification configuration depicted in Fig. 1 contains lateral symmetry with respect to the central line, computations were performed for one of the symmetric halves in order to reduce the overall computational time. The boundary conditions for solving momentum and energy conservation equations (2), (3), and (5) are given as follows: (1) at the top face—$\partial u/\partial y = 0$, gauge pressure $p = 0$, and $\partial T/\partial y = 0$; (2) at the left face (symmetric axis)—$u = 0$, $\partial v/\partial x = 0$, and $\partial T/\partial x = 0$; (3) at the bottom wall—$u = 0$, $v = 0$, and $T = T_b$; and (4) at all the remaining walls—$u = 0$, $v = 0$, and thermally insulated.

III. NUMERICAL APPROACH AND VOLUME FRACTION UPDATING METHODOLOGY

The governing equations [Eqs. (1)–(3) and (5)] associated with fluid flow and heat transfer during directional solidification are in conservative form.[40] They contain a transient term, a diffusive term, a convective term, and source terms pertinent to the physics of the macro-scale solidification process. The finite volume approach of discretization converts this system of parabolic partial differential equations [Eqs. (1)–(3) and (5)] into a system of linear algebraic equations.[40] The systems of these linear algebraic equations are then solved iteratively over the entire domain for each time step. A semi-implicit iterative method is used for solving the coupled velocity and temperature fields. The coefficients associated with the combined convection and diffusion terms are formulated using a power law scheme.[37,40] Although the power law scheme[37,40] is more complicated as compared to the hybrid scheme in implementation, it is computationally less expensive and provides a better representation of exponential behavior observed for the combined convection–diffusion problems. For 2D analysis, the fourth and fifth source terms appearing on the right-hand side of Eqs. (2) and (3), as well as the second source term appearing on the right-hand side of Eq. (5), are discretized by using an implicit first order upwind scheme. In order to check the accuracy of the first order upwind scheme, few of the initial simulations are also performed, considering the second order upwind scheme (linear upwind difference scheme or LUDS[41]), and the results obtained from these two schemes are compared. However, the difference between the simulated results using the first order and second order upwind schemes is found to be insignificant. Since implementation of the second order upwind scheme is computationally more expensive as compared to the first order upwind scheme, the first order upwind scheme is chosen to handle convective source terms for all subsequent numerical simulations. A line-by-line tridiagonal matrix algorithm (TDMA) solver is used to solve the system of linearly discretized algebraic equations for each of the field variables, namely, u, v, and T. The "Semi-Implicit Method for Pressure Linked Equations Revised" (SIMPLER) algorithm is chosen to solve momentum and continuity equations simultaneously for obtaining the velocity field. The choice of SIMPLER algorithm over the more frequently used SIMPLE algorithm is made to obtain an improved convergence rate of the solver.

For the SIMPLER[40] algorithm, the pressure boundary condition at the top face is applied by setting pressure equal to zero at the inner grid points adjacent to the physical boundary. During the evaluation of pressure correction at these inner grid points adjacent to the physical boundary with constant pressure boundary condition, the source terms S_C and S_P in the discretized linear algebraic pressure correction equation are set to be zero and the coefficient a_P is set to have a very large value ($\sim 10^{30}$).[37,40] As a result, the combined effect of other coefficients (a_E, a_W, a_N, and a_S) is suppressed in the discretized linear algebraic pressure correction equation, and the numerically attained pressure correction values are ~0. The vertical velocity component v at the location of the zero gauge pressure boundary condition is computed by using mass conservation at the grid points ($v_N + u_E - v_S - u_W = 0$).[37]

For 3D analysis, the user defined function for the source terms corresponding to momentum equations was incorporated in ANSYS 18.1. The default energy equation of ANSYS was turned off, and instead, Eq. (5) is implemented by declaring T as the user defined scalar. The gradients present in the source terms were evaluated using the Green–Gauss cell based method.[42] For each time step, the velocity field is predicted first from the guessed pressure, density, and volume fractions, followed by the prediction of the temperature field. Finally, phase volume fractions and densities are re-evaluated using the newly updated temperature field. For each time step, iterations are continued until velocity

and temperature satisfy the absolute convergence criteria[43] of 10^{-5} and 10^{-6}, respectively.

The volume fraction updating method is somewhat trivial for the continuous solidification process of the amorphous material defined by the fixed values of liquidus (T_L) and solidus (T_S) temperatures. However, for solidification of a pure substance with a distinct solid–liquid interface, updating of g_l is not trivial and calls for a novel numerical scheme. For the present work, g_l updating methods are derived for both continuous and distinct interface type solidification processes.

For the continuous solidification process, g_l is defined as follows:

$$g_l = \begin{cases} 1 & \text{for } T \geq T_L \\ 0 < g_l < 1 & \text{for } T_S < T < T_L \\ 0 & \text{for } T \leq T_S. \end{cases} \tag{6}$$

The liquid volume fraction (g_l) at a node point is simply calculated as follows:

$$\left(g_{l_P}\right)_{n+1} = \frac{(T_P)_n - T_S}{T_L - T_S}. \tag{7}$$

However, to ensure numerical convergence, the following iterative formulation is considered:

$$\left(g_{l_P}\right)_{n+1} = \left(g_{l_P}\right)_n + \lambda\left[\frac{(T_P)_n - T_S}{T_L - T_S} - \left(g_{l_P}\right)_n\right], \tag{8}$$

where subscript P represents the node point, subscripts n and $n+1$ denote subsequent iteration steps, and λ is an under-relaxation factor.

Updating of g_l is, however, more demanding when solidification of a pure substance with a distinct solid–liquid interface and a constant freezing point needs to be addressed. For solidification of a pure substance, the liquid phase enthalpy is defined as $h_l = (c_{ps} - c_{pl})T_m + h_{sl} + c_{pl}T$, with T_m being the distinct freezing temperature. Thus, T_S appearing in the last source term on the right-hand side of the energy equation [Eq. (5)] has to be replaced with T_m. For solidification with the distinct interface, the volume fraction at the liquid, solid, and interface region is defined as follows:

$$g_l = \begin{cases} 1 & \text{for } T > T_m + \varepsilon \\ 0 \leq g_l \leq 1 & \text{for } T = T_m \pm \varepsilon \\ 0 & \text{for } T < T_m - \varepsilon, \end{cases} \tag{9}$$

where ε is a small number ($O \sim 10^{-6}$), a physical representation of permissible overheating or under-cooling at the interface location.[19] The volume fraction updating is derived on the basis of a similar approach proposed by Voller and Prakash.[15] To obtain an exclusive relation to update g_l, Eq. (5) is discretized into a linear algebraic equation using the finite volume method and is given as follows:

$$\begin{aligned}\left(a_P + a'_P\right)T_P = {} & \sum\left(a_{nb} + a'_{nb}\right)T_{nb} + A^0_P g^0_{l_P} - A_P g_{l_P} \\ & + B^0_P g^0_{l_P}(\rho_l T^0_P - \rho_s T_m) - B_P g_{l_P}(\rho_l T_P - \rho_s T_m) + a^0_P T^0_P.\end{aligned} \tag{10}$$

a'_P and a'_{nb} appearing in Eq. (10) are the coefficients obtained by discretizing the second term on the right-hand side of Eq. (5) using the first order upwind scheme, whereas a_P and a_{nb} are evaluated using the power law scheme defined by Patankar[40] and superscript 0 denotes previous time step values. Noting $a_P = a_E + a_W + a_N + a_S + a^0_P$, Eq. (10) can be rearranged and expressed for the nth iteration step as follows:

$$a^0_P(T_P)_n = (A)_n + (B)_n + (C)_n + (D)_n, \tag{11}$$

where

$$(A)_n = \sum\left(a_{nb} + a'_{nb}\right)_n (T_{nb})_n - \left(a_E + a_W + a_N + a_S + a'_P\right)_n (T_P)_n, \tag{12}$$

$$(B)_n = A^0_P g^0_{l_P} + B^0_P g^0_{l_P}\left(\rho_l T^0_P - \rho_s T_m\right) + a^0_P T^0_P, \tag{13}$$

$$(C)_n = -(A_P)_n\left(g_{l_P}\right)_n, \tag{14}$$

$$(D)_n = -(B_P)_n\left(g_{l_P}\right)_n(\rho_l T_P - \rho_s T_m)_n. \tag{15}$$

Similarly, for the $n+1$th iteration step, Eq. (10) is reordered as

$$a^0_P(T_P)_{n+1} = (A)_{n+1} + (B)_{n+1} + (C)_{n+1} + (D)_{n+1}, \tag{16}$$

where $(A)_{n+1}$, $(B)_{n+1}$, $(C)_{n+1}$, and $(D)_{n+1}$ are evaluated by replacing n with $n+1$ in Eqs. (12)–(15). By subtracting Eq. (16) from Eq. (11) and noting $(B)_{n+1} = (B)_n$, we obtain

$$\begin{aligned}a^0_P((T_P)_n - (T_P)_{n+1}) = {} & [(A)_n - (A)_{n+1}] + [(C)_n - (C)_{n+1}] \\ & + [(D)_n - (D)_{n+1}].\end{aligned} \tag{17}$$

At this point, a drastic measure of dropping the first term on the right-hand side of Eq. (17) involving convection–diffusion terms is taken. At first glance, dropping of the convection–diffusion term looks severe; however, in an iterative framework, this decision leads to a permissible and convenient updating method for g_l. Dropping the combined convection–diffusion flux effects renders Eq. (17) to retain only the transient terms,

$$a^0_P((T_P)_n - (T_P)_{n+1}) = [(C)_n - (C)_{n+1}] + [(D)_n - (D)_{n+1}]. \tag{18}$$

A_P, B_P, and a^0_P appearing in Eqs. (10)–(18) are given as follows:[40]

$$A_P = \frac{\rho_s h_{sl}}{c_{ps}}\frac{\Delta x \Delta y}{\Delta t}, \quad B_P = \left(\frac{c_{pl}}{c_{ps}} - 1\right)\frac{\Delta x \Delta y}{\Delta t}, \quad \text{and} \quad a^0_P = \frac{\rho^0_p \Delta x \Delta y}{\Delta t}. \tag{19}$$

Noting [from Eq. (19)] that $(A_P)_n = (A_P)_{n+1}$ and $(B_P)_n = (B_P)_{n+1}$ and substituting expressions of C and D from Eqs. (14) and (15) into Eq. (18), the following expression is obtained for updating g_l:

$$\left(g_{l_P}\right)_{n+1} = \left(g_{l_P}\right)_n + \frac{\left[B_P \rho_l \left(g_{l_P}\right)_n + a^0_P\right]((T_P)_n - (T_P)_{n+1})}{A_P + B_P(\rho_l (T_P)_{n+1} - \rho_s T_m)}. \tag{20}$$

An elementary control volume undergoing the solidification process needs to satisfy the condition of attaining the freezing temperature T_m. Thus, $(T_P)_{n+1}$ is chosen to be T_m in Eq. (20). Additionally, an under-relaxation factor λ is multiplied with the second term appearing on the right-hand side of Eq. (20). As a result, $(g_{l_P})_{n+1}$ is evaluated by adding a correction factor with the previous iteration value $(g_{l_P})_n$,

$$\left(g_{l_P}\right)_{n+1} = \left(g_{l_P}\right)_n + \lambda\frac{\left[B_P \rho_l \left(g_{l_P}\right)_n + a^0_P\right]((T_P)_n - T_m)}{A_P + B_P T_m(\rho_l - \rho_s)}. \tag{21}$$

Equations (8) and (21) provide the required volume fraction updating formulations for solidification processes associated with continuous and distinct interface solid front growth. Finally, considering the fact that the physical value of the volume fraction remains within the range $0 \le g_l \le 1$, values of g_l obtained from the proposed formulation [Eqs. (8) and (21)] are restricted to exist within this permissible range by assigning the following conditions:

$$\left(g_{l_P}\right)_{n+1} = \begin{cases} 1 & \text{if } \left(g_{l_P}\right)_{n+1} > 1 \quad \text{from Eqs. (8) or (21)} \\ 0 & \text{if } \left(g_{l_P}\right)_{n+1} < 0 \quad \text{from Eqs. (8) or (21).} \end{cases} \tag{22}$$

Thus, a very comprehensible volume fraction updating scheme [Eqs. (8), (21), and (22)] is developed, which allows us to estimate the volume fraction ahead of calculating the velocity and temperature fields.

IV. EXPERIMENTAL SETUP

To validate the numerical results associated with the proposed shrinkage induced flow model, an experimental setup is designed and fabricated to study the solidification of coconut oil in a bottom cooled configuration. The experiments are performed to obtain both qualitative and quantitative validation. One of the major limitations of the present numerical model is its incapability of capturing the evolution of free surface (the interface between liquid and air at the top of the riser). Thus, the riser needs to have a steady supply of the melt from a larger reservoir during the solidification process. Suitable arrangements are incorporated in the experimental setup to meet this particular feature.

The schematic of the experimental setup is shown in Fig. 2. The experimental setup consists of a rectangular cavity divided into an upper and a lower cell by a thick acrylic glass. The acrylic glass separating the two cavities contains a through and through square hole at the center, which acts as a connecting riser between the upper and lower cavities. The upper cavity serves as the melt reservoir, while the lower one represents the solidification cell. The bottom most surface of the lower cavity is cooled below the solidus temperature (T_S) of coconut oil and solidification ensues from this surface. All the side walls of the cavity are adequately insulated by maintaining an air gap between the inner wall and the outer wall of the central cavity.[35]

The flow physics associated with shrinkage induced convection is similar for all three types of solidification processes (distinct interface type, continuous, and alloy solidification). However, coconut oil is chosen on the basis that (a) it is transparent in the liquid phase, (b) the range of freezing temperature is close to room temperature (T_L = 300 K and T_S = 294 K for coconut oil), and (c) the density difference between solid and liquid phases is fairly large ($\rho_s - \rho_l$ = 60 kg/m^3) to induce shrinkage driven flow during the solidification process. Since the velocity field in the melt is captured by using PIV, transparency of the liquid phase is an absolute necessity for the experimental visualization of the velocity field.

The inner and outer walls of the cavity are built using an acrylic glass of 8 mm thickness. The dimension of the rectangular inner cavity is 65 × 35 × 80 mm^3 (length × thickness × height), and the overall dimension of the rectangular exterior of the setup is 101 × 71 × 70 mm^3. Provision is made to separate the inner cavity into upper and lower chambers by means of placing a solid block acrylic glass of dimension 65 × 35 × 15 mm^3 inside the cavity. The solid block connecting the upper and lower cavities contains a square hole of 3 × 3 mm^2 through the block at the center and is merely the minimum geometrical constraint achievable by the laser cutter. The square hole connecting the upper and lower cavities functions as a riser and allows the fluid to flow from the upper to lower cavity to compensate for the shrinkage of the melt encountered in the lower cavity due to the ongoing solidification process in it. The vertical positioning of the separating solid block with the riser hole is made adjustable so that the volume of the reservoir and the solidification chamber can be altered as per the experimental requirements. Solidification is obtained by maintaining the cooling temperature ($T_b < T_S$) of a 2 mm thick Cu plate located at the bottom of the lower cavity. In order to maintain a fixed cooling temperature T_b at the bottom surface of the lower cavity, Peltier modules (thermo-electric cooler modules) integrated with a Cu chill heat exchanger[34,44] is used. The thermal conductivity of the acrylic glass is very low (<0.2 W/mK). The air gap maintained between the inner and outer walls all around the cavity enhances the insulation further, causing negligible heat transfer from the surrounding. For flow visualization in the melt, the liquid coconut oil initially occupying the lower solidification chamber and the upper reservoir cavity is seeded with neutrally buoyant hollow glass spheres of 10 μm average diameter. Once solidification ensues from the bottom most surface of the lower cavity, the particle image velocimetry (MicroVec PIV®) technique is used to capture the velocity field in the melt.[34,44]

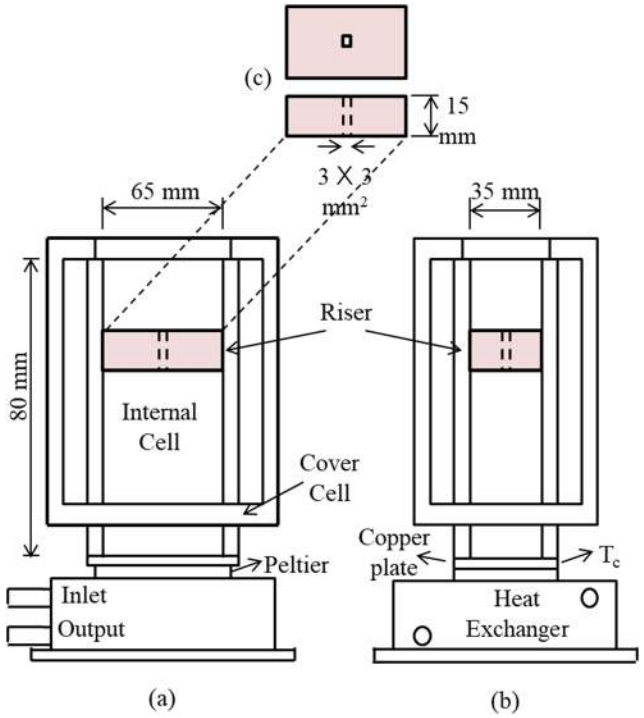

FIG. 2. Schematic of the experimental setup: (a) front view, (b) side view, and (c) riser.

A. Experimental procedure

Coconut oil is heated to a temperature of 308 K to make sure that at the initial state, it is in the pure liquid phase. The ambient temperature in the room is controlled and maintained at 308 K using a number of heaters and thermostats. Seed particles are added into the liquid coconut oil at 308 K and stirred until uniform distribution of seed particles in the melt is obtained. The seeded liquid coconut oil is then poured into the rectangular cavity and stirred thoroughly, ensuring that no air pocket is trapped in the liquid at any part of the cavity. The separating block containing the connecting through and through hole is then placed. The position of the separating block is adjusted to obtain the desired volume of the solidification chamber. As the solidification process ensues and continues, images of the 2D field obtained from the laser–mirror arrangement[34,35] are captured continuously using a charged coupled device (CCD) camera (Imperx CLB-B2520M, resolution 2456 × 2048). PIV images are captured using the magnification of 8× and a pulse width of 125 ms. While evaluating the velocity field from the images using MicroVec PIV software, an interrogation window of 64 × 32 pixel^2 was chosen.[34,44,45] The sequential image data are stored in a memory drive, and TECPLOT software is used for data processing and velocity field image recreation. During the experiments, the bottom surface temperature of the solidification cell is maintained at 258 K.

V. RESULTS AND DISCUSSION

This section is divided into three subsections. Section V A involves the comparison of the 2D shrinkage induced flow with and without considering the buoyancy effect. The shrinkage induced flow analysis reported by Chiang and Tsai[21] involving directional solidification from the bottom was devoid of the buoyancy effect consideration. Our first objective is to check the merit of this particular assumption in predicting the shrinkage induced flow field. The analysis involves obtaining the shrinkage induced flow field and solid front growth during directional solidification of pure Al in a bottom cooled configuration. The results obtained in this subsection shows that inclusion of the buoyancy source term alters the flow field significantly as opposed to that obtained without including the buoyancy effect.

Section V B is attributed to the experimental validation of the flow phenomena obtained from the numerical results in Sec. V A. The experimental validation involves directional solidification of coconut oil in a bottom cooled configuration. Qualitative and quantitative validation of the proposed model is discussed in this subsection. Section V C is attributed to the 2D case studies involving solidification of pure Cu and Al to verify the generality of this newly found flow orientation. The study involving directional solidification of Al is revisited with varying parameters such as cold boundary temperature, initial temperature, and cavity aspect ratio.

A. Comparison of 2D shrinkage models with and without considering buoyancy effect

Numerical analysis is carried out for directional solidification of pure Al in a bottom cooled configuration considering (a) exclusion of the buoyancy effect on the flow field[21] and (b) inclusion of the buoyancy effect on the flow field. The properties of pure Al are shown in Table I along with casting conditions and cavity geometry details. In order to study grid independence, analysis is carried out for three different grid sizes, namely, 60 × 90, 80 × 120, and 100 × 150 for the symmetry half. Similarly, the time step independence is checked by considering three different time steps, namely, Δt = 0.25 s, 0.5 s, and 1.0 s. The maximum velocity (v_{max}) within the fluid domain and the interface position (y_{int}) from the bottom surface of the cavity along the symmetry-axis obtained at the time instant 10 s are compared and tabulated in Table II for different grid sizes and time steps. No significant difference in results is found above grid size 80 × 120 and time step below Δt = 0.5 s (the results differ within 1% error limit). Hence, a grid size of 80 × 120 grids and a time step Δt = 0.5 s are used for most of the 2D case studies. For the case studies involving varying aspect ratios of the cavity, the grid size is modified in a proportionate manner. Figure 3 shows velocity fields and solid fronts at different stages of solidification when the buoyancy effect is not considered. For this case study, flow fields similar to that described by Chiang and Tsai[21] are obtained (Fig. 3). The flow fields shown in Fig. 3 are characterized by a single descending fluid column coming straight down from the riser, which eventually collides head on with the growing solid front before getting bifurcated into two counter-rotating convection cells. The maximum velocity within the flow field is mentioned at the top of the each figure.

On the other hand, when the buoyancy effect is taken into account, the evolution of the flow field shown in Fig. 4 indicates a distinctively different flow pattern. As is evident from the flow fields shown in Fig. 4, the fluid column entering the cavity from the riser

TABLE I. Material properties of Al,[46,47] casting conditions, and geometrical data for numerical analysis.

k_l = 90.7 W/mK	k_s = 211 W/mK
c_{pl} = 1087 J/kg K	c_{ps} = 1203 J/kg K
ρ_l = 2370 kg/m^3	ρ_s = 2535 kg/m^3
h_{sl} = 398 000 J/kg[a]	$\beta = 2.1 \times 10^{-5}$ K^{-1}[a]
$\mu = 1.38 \times 10^{-3}$ kg/ms	T_m = 933.2 K
T_i = 1073 K	T_b = 800 K
W_c = 200 mm	H_c = 100 mm
W_R = 20 mm	H_R = 50 mm

[a]Assumed.

TABLE II. Grid independence study for 2D numerical analysis at 10 s; comparison of the maximum flow velocity v_{max} and the solid–liquid interface location y_{int}.

Grid size \ Time step		0.25 s	0.5 s	1 s
60 × 90	v_{max} (mm/s)		1.114	
	y_{int} (mm)	...	17.32	...
80 × 120	v_{max} (mm/s)	1.101	1.080	0.912
	y_{int} (mm)	17.511	17.557	17.797
100 × 150	v_{max} (mm/s)		1.091	
	y_{int} (mm)	...	17.472	...

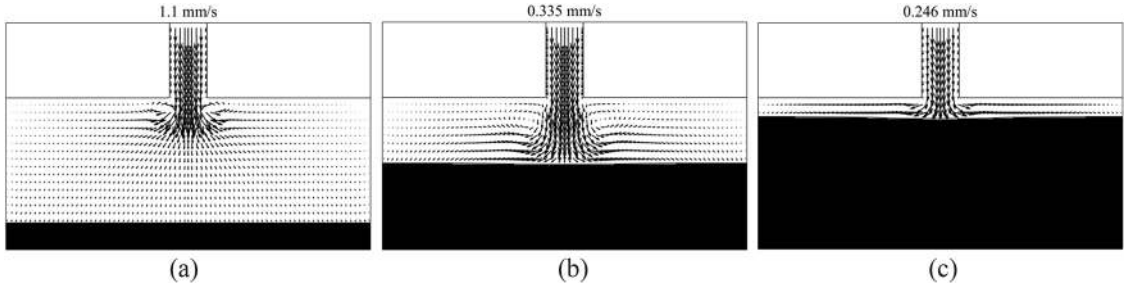

FIG. 3. Shrinkage induced flow field during solidification of pure Al in a bottom cooled configuration without considering the buoyancy effect at (a) 10 s, (b) 100 s, and (c) 200 s.

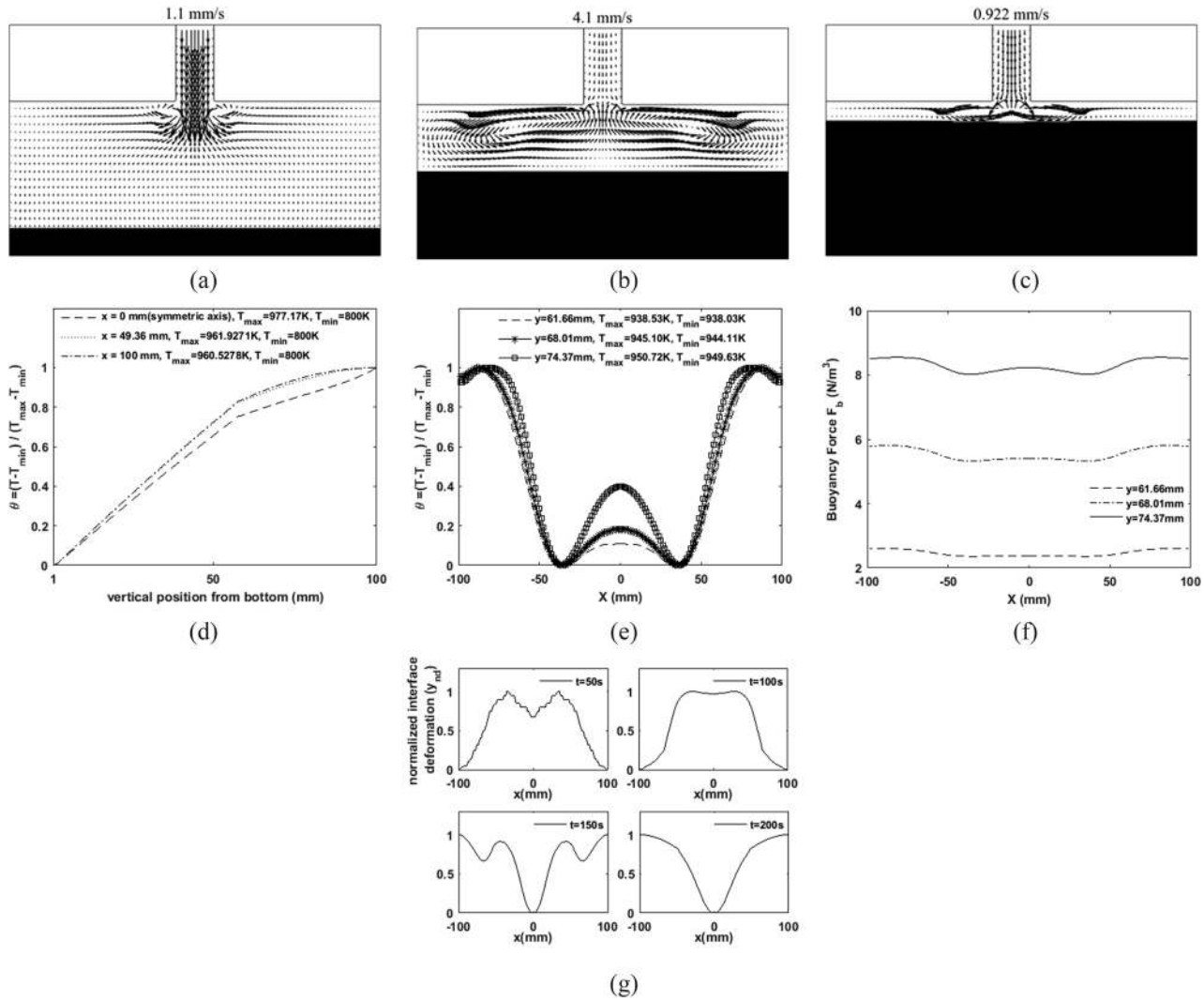

FIG. 4. Shrinkage induced flow field during solidification of pure Al in a bottom cooled configuration considering the buoyancy effect at (a) 10 s, (b) 100 s, and (c) 200 s, and the (d) temperature profile in the y-direction at constant x-locations and 100 s, (e) near interface temperature deformation in the x-direction at constant y-locations and 100 s, (f) buoyancy force (per unit volume): $\rho^{l}_{ref} g_a \beta (T - T_{ref})$ variation in the x-direction at constant y-locations and 100 s, and (g) normalized interface deformation $(y_{nd} = (y_{int} - y_{int_{min}})/(y_{int_{max}} - y_{int_{min}}))$ at different times, where y_{int} represents the height of the interface from the bottom surface of the cavity.

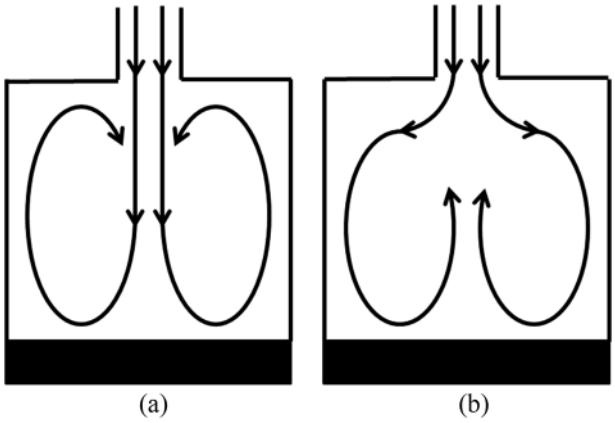

FIG. 5. Schematic of flow physics obtained (a) without accounting for the buoyancy effect and (b) considering the buoyancy effect.

cannot penetrate deeper into the melt region of the cavity. Instead, the incoming fluid column gets bifurcated in the lateral direction just after entering the cavity to once again produce a pair of counter-rotating convection cells. However, the counter-rotating convection cells obtained from this analysis have exactly opposite directionality as compared to those obtained from the no buoyancy effect consideration. Figure 5 provides a schematic representation of the two different flow fields obtained from these two analyses. For the bottom cooled configuration, the density field is stably stratified. As a result, cold and heavier fluid layers adjacent to the growing solid front resist the downward movement of the hot and lighter incoming fluid from the riser. In essence, the stably stratified buoyancy field opposes the shrinkage induced flow to penetrate deeper into the melt region. Consequently, the incoming fluid from the riser is forced to take a least resistant lateral path at an early stage of its descent from the riser. As a result, the incoming flow from the riser is bifurcated at a region adjacent to the riser opening, forming a pair of counter-rotating convection cells in the 2D plane. The very nature of the flow causes the heavier cold fluid close to the solid front to rise along the central column and collide head on with the down-coming flow from the riser opening, leading to the sustenance of this typical flow field. From the comparison of flow fields obtained after 10 s without and with the buoyancy effect [Figs. 3(a) and 4(a)], both the flow fields look identical with partial penetration of the descending fluid column from the riser opening into the cavity. However, at later stages of solidification [Figs. 3(b), 3(c), 4(b), and 4(c)], the flow fields obtained from these two case studies exhibit a highly contrasting flow reversal pattern.

Since the bottom cooled orientation typically provides a stably stratified density field in the vertical direction, the effect of buoyancy can only be evident if there exists non-horizontal isotherms along the x direction. Figures 4(d) and 4(e) show the vertical and horizontal non-dimensional temperature profiles at chosen values of x and y coordinate locations, respectively, at time instant 100 s. As is evident, the vertical temperature profiles represented by Fig. 4(d) indicate the stably stratified density field along the vertical direction (low temperature corresponding to higher density and high temperature corresponding to lower density). However, the temperature profile in the horizontal direction is found to be undulated, justifying the significance of the buoyancy effect. We should note here that the non-dimensional temperature [in Figs. 4(d) and 4(e)] is executed by considering the maximum and minimum temperatures along the chosen vertical and horizontal lines only and not through global maximum or minimum temperatures. A close view of Fig. 4(e) indicates that the differences between these maximum and minimum temperatures are found to be quite small (typically of the order of 0.1–1 K). Evidently, the buoyancy force variation along the horizontal direction although small is nevertheless existing [Fig. 4(f)]. At first glance, the buoyancy force profile along the horizontal direction [Fig. 4(f)] gives an impression that the coupling torque should give rise to a pair of vortices with the fluid coming down along the center line and rising along the side walls, which contradicts our present observation. However, we must remember that it is the combined effect of shrinkage and buoyancy that defines the flow field. As we have mentioned earlier, the incoming flow from the riser containing the hot lighter fluid being unable to penetrate the colder heavy liquid layers lying immediately underneath chooses lateral paths with less flow resistance and is driven toward the side walls. Adjacent to the side walls, the shrinkage induced flow has no other option but to flow in the downward direction along the wall. The inertia of this shrinkage induced downward flow counteracts the fluid region having higher buoyancy, nullifying the buoyancy effect in that region. On the other hand, the buoyancy force in the vicinity of the cavity central line does not get counteracted by any such means. The inertia of the rerouted shrinkage induced flow following the cavity profile along the walls and interface toward the central line of the cavity ends up assisting the buoyancy force adjacent to the cavity center to lift the fluid from the interface along the center line. Figure 4(g) provides a close-up view of the interface profile along the horizontal direction at different time intervals. All these interface shapes are characterized by the presence of a central depression. This central depression becomes more and more prominent as the solid front grows with the passage of time. The minuscule deformation of isotherms adjacent to the central depression of the interface aided by the inertial effect of the rerouted shrinkage induced flow causes the sustenance of reversed flow phenomena. A similar phenomenon was observed during the vertical Bridgman growth with the bottom cooled configuration by Motakef,[48] although the shrinkage induced flow was not as prominent as the present study.

B. Experimental validation

To comprehend the newly found flow physics, 3D numerical and experimental studies were performed considering coconut oil as the phase change material (PCM). The thermo-physical properties of coconut oil reported by Timms[49] are tabulated in Table III along with casting conditions. However, the experimentally measured values of thermal conductivity of solid and liquid phases of coconut oil (k_l and k_s) are considered for the better accuracy of numerical prediction. With the data regarding the thermal expansion coefficient of coconut oil (β) being unavailable in the existing literature, we assumed the numerical value of this parameter for our numerical prediction.

For the experimental analysis, the solid block separating the upper and lower chambers is positioned to maintain the height of the

TABLE III. Material properties of coconut oil and casting conditions for numerical analysis.

$k_l = 0.2004$ W/mK[a]	$k_s = 0.3$ W/mK[a]
$c_{pl} = 2088$ J/kg K	$c_{ps} = 2088$ J/kg K
$\rho_l = 900$ kg/m^3	$\rho_s = 960$ kg/m^3
$h_{sl} = 108\,784$ J/kg	$\beta = 8.9 \times 10^{-4}$ K^{-1}[b]
$\mu = 3.29 \times 10^{-2}$ kg/ms	$T_S = 294$ K
$T_L = 300$ K	$T_i = 308$ K
$T_b = 258$ K	

[a]Measured.
[b]Assumed.

solidification cavity (lower chamber) at 40 mm. The numerical analysis is carried out for the one fourth symmetric portion, cut along the symmetry planes passing through the length and width of the solidification cavity and riser. For 3D analysis, along with Eqs. (1)–(3) and (5), the momentum equation along the z-axis (representing the width of the cavity) is also solved. The z-momentum equation is given as follows:

$$\frac{\partial}{\partial t}(\rho w) + \nabla \cdot \left(\rho \vec{\mathbf{V}} w\right) = \nabla \cdot \left(\mu_l \frac{\rho}{\rho_l} \nabla w\right) - \frac{\partial p}{\partial z} - \frac{\mu_l}{K}\frac{\rho}{\rho_l} w - \nabla \cdot \left(\rho \frac{g_s \rho_s}{g_l \rho_l} \vec{\mathbf{V}} w\right) + \nabla \cdot \left(\mu_l w \nabla\left(\frac{\rho}{\rho_l}\right)\right). \quad (23)$$

The riser cross section is chosen to ascertain the magnitude of fluid velocity within the perceivable range of PIV measurement. For numerical analysis, the grid independence and time step independence study is carried out. Three different grid resolutions are considered. After attaining satisfactory grid independence, three different time steps are considered to investigate the time step independence for the chosen grid resolution. The mass flow rate at the riser inlet at the time instant of 180 s during the solidification is compared for different grid resolutions and time steps, tabulated in Table IV. On the basis of this comparison, the second grid resolution depicted in Table IV with a time step of 0.5 s is selected for the numerical analysis.

The velocity field and liquid–mushy zone interface locations obtained from experiments and numerical analysis are compared and shown in Fig. 6 during different stages of solidification of coconut oil. It is pertinent to mention here that the camera resolution of the PIV system restricted us to capture the entire cavity–riser arrangement. Hence, we chose only the upper portion of the solidification cavity along with the riser as our field of view (L = 65 mm × H = 30.7 mm). The experimental results shown in Figs. 6(a)–6(c) indeed confirm the reversed flow phenomena described by the simplified diagram presented in Fig. 5(b). The qualitative comparisons between the experimentally and numerically attained flow patterns within the melt domain shown in Fig. 6 are found to agree reasonably. A quantitative validation between experimentally and numerically obtained temporal evolution of interface positions and magnitude of maximum velocities within the fluid domain is also carried out and shown in Fig. 7. Although we obtained a very good match between the experimentally measured and numerically determined interface location, the comparison of maximum absolute velocity is found out to be reasonable in terms of order of magnitude. The mismatches between experimental and numerical results can be attributed to the probable differences between the real and assumed values of thermo-physical properties, uncertainties associated with experiments, marginal errors in geometric considerations, and minor heat losses through the side walls.

Unlike the 2D case study involving bottom cooled directional solidification of pure aluminum, the flow reversal phenomena are found to be dominant from the very inception of the solid front growth during directional solidification of coconut oil in bottom cooled orientation. Liquid aluminum being a metal with significantly high thermal conductivity has a very low Prandtl number ($Pr = 0.0165$). The strength of Pr signifies the ability of the flow field to perturb the thermal field. With the Prandtl number of liquid aluminum being very small, perturbation of the thermal field due to the shrinkage induced flow during directional solidification of aluminum is expected to be minuscule. However, minute deformation of isotherms due to the emergence of central depression of the solid–liquid interface [Fig. 4(g)] causes the unbalanced buoyancy force adjacent to the cavity central region to initiate the flow reversal phenomena. The flow reversal phenomenon for bottom cooled directional solidification of aluminum does not occur until the emergence of the central depression on the solid–liquid interface. On the other hand, the Prandtl number for coconut oil is found out to be quite large ($Pr = 342.8$), suggesting the possibility of significant deformation of the thermal field due to the existing flow field.

TABLE IV. Grid independence study for the 3D numerical analysis at time 180 s.

Grid size \ Time step	0.1 s	0.5 s	1 s
$(36 \times 20 \times 40)$[a] + $(4 \times 4 \times 16)$[b]	4.4504×10^{-7} kg/s	...	...
$(54 \times 30 \times 60)$[a] + $(6 \times 6 \times 24)$[b]	4.4532×10^{-7} kg/s	4.4508×10^{-7} kg/s	4.4323×10^{-7} kg/s
$(63 \times 35 \times 70)$[a] + $(7 \times 7 \times 28)$[b]	4.5397×10^{-7} kg/s	...	...

[a]Grid resolution for the cavity.
[b]Grid resolution for the riser.

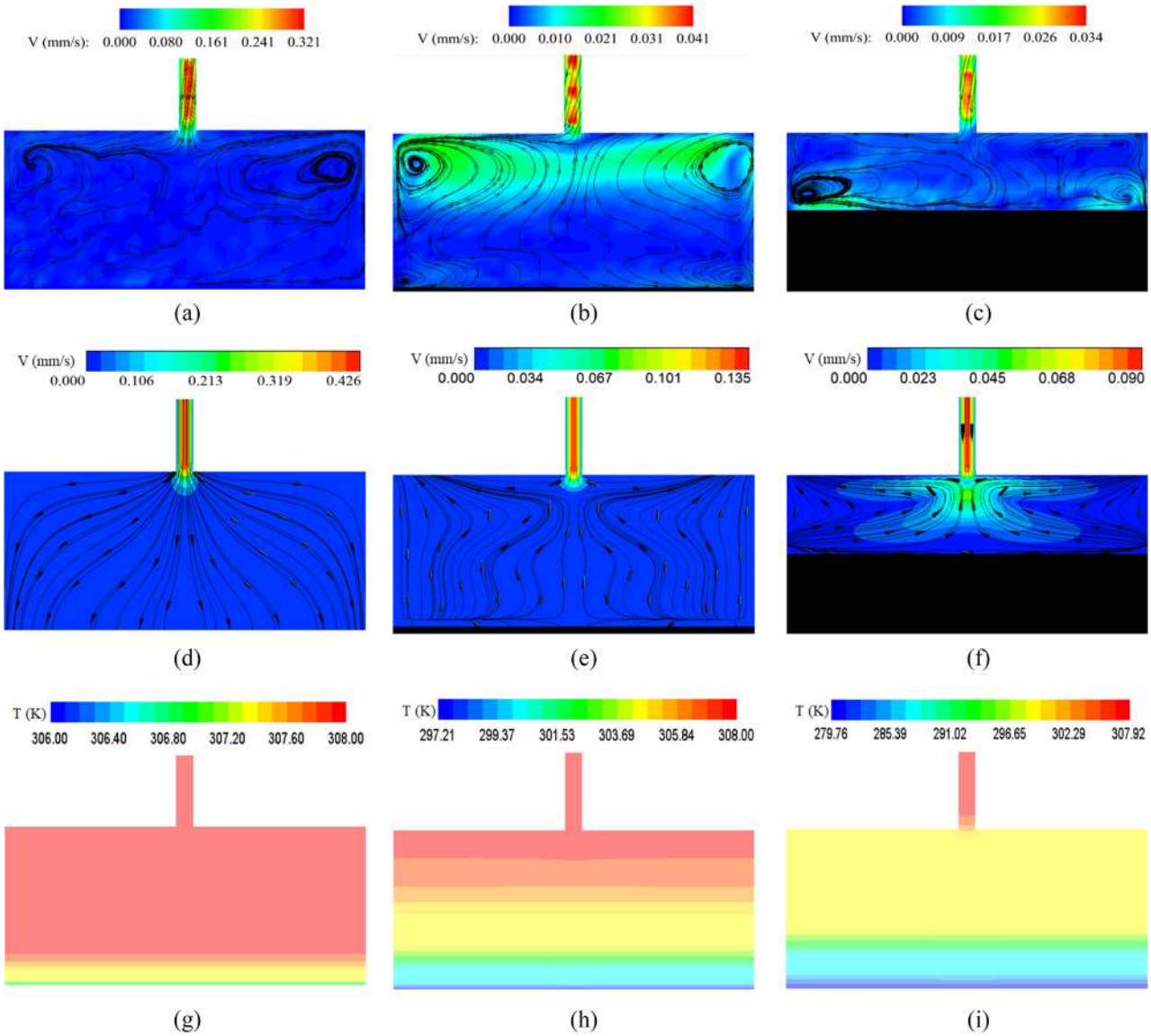

FIG. 6. Experimentally measured velocity field and mushy–liquid interface location at (a) 180 s, (b) 1200 s, and (c) 4500 s; numerically obtained velocity field and mushy–liquid interface location at (d) 180 s, (e) 1200 s, and (f) 4500 s; and temperature field at (g) 180 s, (h) 1200 s, and (i) 4500 s, respectively.

As a result, an undulated buoyancy field along the horizontal direction can be achieved even before the emergence of the non-planar growth of the solid front, and flow reversal is prominent from the very instance of the solid front growth.

The interaction between the convection field and the liquid–mushy interface causes the interface to deviate from the planar growth. Deformation of the planar interface in the form of a plunge pool with length- and width-wise orientation is observed during the experiments. Figures 8(a) and 8(b) show the orientation of these plunge pools during two different sets of experiments. The numerical simulations could capture these experimentally manifested plunge pools with limited accuracy [Fig. 8(c)]. However, the numerical prediction of the plunge pool is obtained after a time lag of approximately 120 s, as compared to the experimental observations. The orientation of the plunge pools shown in Figs. 8(b) and 8(c) is found to be similar in nature. The particular orientation of the plunge pool can be attributed to the square cross section of the riser, which allowed the shrinkage induced flow to align along the length and width of the cavity. The shrinkage induced deformity of the planar mushy front in the form of a distinctively oriented plunge pool might lead to interesting compositional heterogeneity during the solidification of alloy systems.

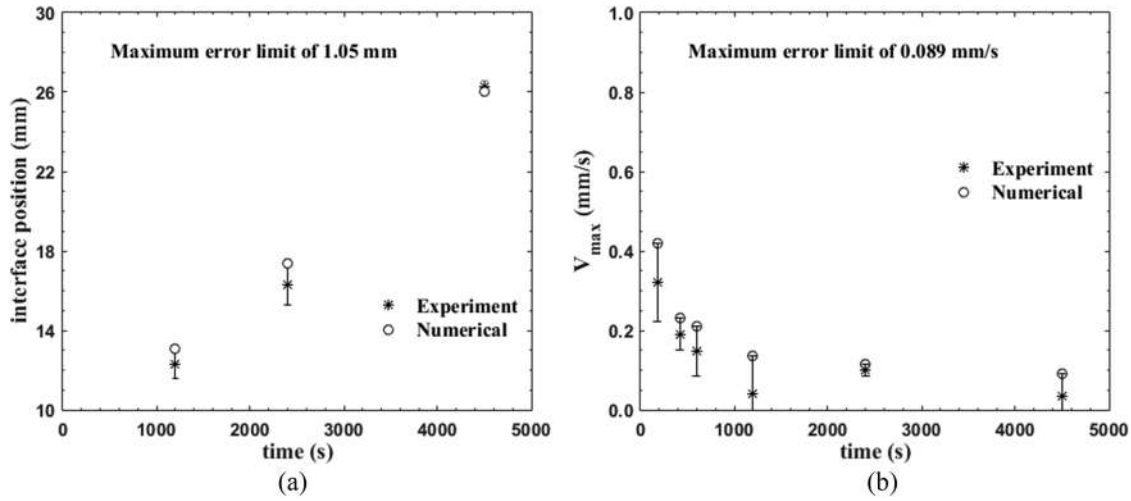

FIG. 7. Comparison between the experimentally and numerically obtained temporal variation of (a) interface position and (b) maximum velocity within the melt domain.

However, directional alloy solidification is beyond the scope of this work.

C. Case studies

Once confidence on the proposed model is established through the experimental validation, analysis is performed considering directional solidification in bottom cooled orientation for one more pure metal, namely, Cu, to check the generality of the proposed model. Finally, solidification of Al for various cold boundary temperatures, initial conditions, and cavity heights is analyzed.

1. Directional solidification of pure Cu

The associated thermo-physical properties and geometric data for Cu are provided in Table V[50,51] The same mesh size and time step used for the 2D analysis concerning solidification of pure Al in Sec. V A is used for this analysis. The initial temperature T_i and cold boundary temperature T_b for the analysis are selected in such a way that $T_i - T_m \approx 140$ K and $T_m - T_b \approx 133$ K. Figure 9 shows the evolution of the velocity field and interface growth at time instants 10 s, 24 s, and 100 s. The temporal evolution of the velocity field is found to be quite similar to that obtained for pure Al, as shown in Fig. 9. The flow field at an early stage is characterized by a pair of counter-rotating convection cells adjacent to the riser opening with the central plane flow directed in the downward direction [Figs. 9(a) and 9(b)]. At later stages of solidification, these counter-rotating convection cells reverse their direction, causing a net upward flow along the central plane toward the riser opening due to the effect of buoyancy. However, the magnitude of maximum velocity due to the shrinkage induced flow during the directional

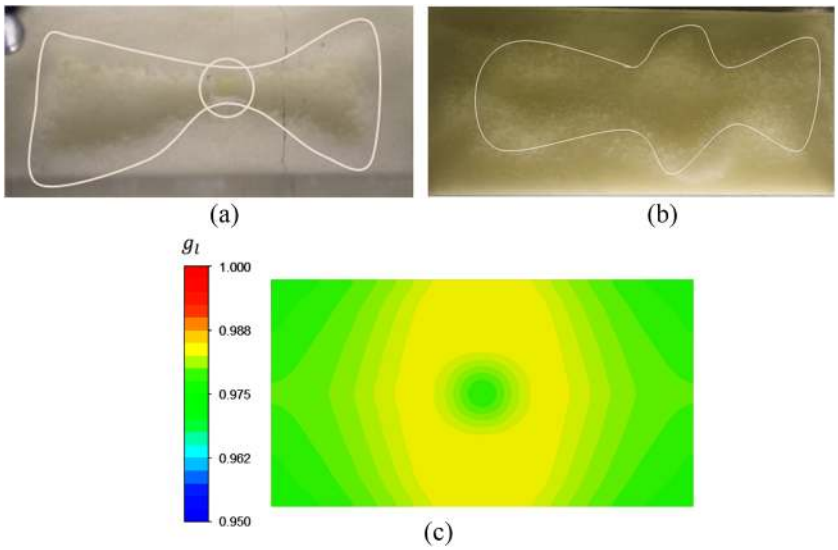

FIG. 8. Plunge pool orientation obtained from the top view at the mushy–liquid interface caused by convection penetration for (a) experiment 1 at 5400 s and (b) experiment 2 at 5400 s. (c) Numerically predicted liquid volume fraction on the interface plane at 5520 s.

TABLE V. Material properties of Cu along with casting conditions for numerical analysis.

k_l = 180 W/mK	k_s = 390 W/mK
c_{pl} = 490 J/kg K	c_{ps} = 390 J/kg K
ρ_l = 7881 kg/m^3	ρ_s = 8790 kg/m^3
h_{sl} = 206 000 J/kg	β = 0.000 016 K^{-1}
μ = 0.003 21 kg/ms	T_m = 1356 K
T_i = 1496 K	T_b = 1223 K
W_c = 200 mm	H_c = 100 mm
W_R = 20 mm	H_R = 50 mm

solidification of Cu is found to be higher as compared to the case study associated with Al. Since the density difference between solid and liquid phases ($\rho_s - \rho_l$) of Cu (≈909 kg/m^3) is much larger than Al (≈165 kg/m^3), the shrinkage induced pull is expected to be much more in the case of solidification of Cu, leading to larger velocity magnitudes.

2. Effect of varying cold boundary temperature

This study is conducted for directional solidification of Al in bottom cooled orientation considering three different cooling temperatures applied at the bottom surface, viz., 300 K, 600 K, and 800 K, while keeping the same geometrical constraints of the cavity provided in Table I. One of the major objectives of this study is to analyze the onset of flow reversal phenomena with respect to the normalized time scale for solidification. The colder the bottom surface temperature, the faster the solidification rate. The time duration required for the completion of solidification in the cavity for each cold boundary condition is predicted and considered to be 100%. The time scale is normalized by dividing time with the total time duration to accomplish complete solidification in the cavity for individual cold boundary temperatures. This method enabled us to predict the percentage of total time duration the liquid melt encounters the forward [Fig. 5(a)] and reverse [Fig. 5(b)] convection pattern. A close inspection of velocity fields presented in Figs. 4 and 9 reveals that all the velocity vectors along the central symmetry line of the cavity are pointing in the downward direction when the forward flow condition [Fig. 5(a)] prevails. On the other hand, all velocity vectors in a bounded region along the central symmetry line manifest upward fluid movement during the reverse flow condition. The location of this bounded sub-region with the upward pointing velocity vector may vary along the central line span depending on varying cold boundary conditions, initial conditions, and cavity aspect ratios. Nevertheless, this particular flow feature always prevails under the reverse flow condition. In essence, when all velocity vectors along the central symmetry line are pointing in the downward direction, we have the forward flow condition [Fig. 5(a)], and all velocity vectors within a bounded sub-region along the central symmetry line pointing upward signifies the reverse flow condition [Fig. 5(b)]. A magnified view of the velocity vectors along the central symmetry plane for the forward and reverse flow is illustrated in Fig. 10(a). The onset of flow reversal phenomena can be apprehended by the sudden change in the velocity vector direction from down to up for a bounded sub-region along the central symmetry line. A sorting algorithm is used at each time instant to identify the direction of velocity vectors along the symmetry line. If all the vectors point in the downward direction ($-ve$ v component), the velocity at the midpoint between the interface and the upper surface of the cavity is stored for that particular time instant. On the other hand, if a bounded sub-region is identified with upward velocity vectors ($+ve$ v component), the velocity at the midpoint of the sub-region is stored for that time instant. This sorting process at progressive time intervals enables us to obtain a single representative velocity vector ($\vec{\mathbf{v}}_{ref}$) for each time instant in such a way that the sign of this single velocity vector solely determines whether the flow phenomena are forward or reverse. This sorting process also leads to easy identification of the time instant when the sign of the $\vec{\mathbf{v}}_{ref}$ changes from $-ve$ to $+ve$, denoting the onset of the flow reversal process. It is pertinent to mention here that the sign of the $\vec{\mathbf{v}}_{ref}$ emphasizes the onset of flow reversal, while the magnitude is of no consequence whatsoever. Therefore, the magnitude of the $\vec{\mathbf{v}}_{ref}$ is normalized within a range of ±1 to describe the flow reversal phenomena in Fig. 10(b). The normalized representative velocity vector $\vec{\mathbf{v}}_{rn}$ is defined as follows:

$$\vec{\mathbf{v}}_{rn} = \begin{cases} \vec{\mathbf{v}}_{ref}/|\vec{\mathbf{v}}_{ref}^{min}| & \text{if} \quad \vec{\mathbf{v}}_{ref} < 0 \\ \vec{\mathbf{v}}_{ref}/|\vec{\mathbf{v}}_{ref}^{max}| & \text{if} \quad \vec{\mathbf{v}}_{ref} > 0. \end{cases} \tag{24}$$

The onset of flow reversal with respect to the normalized time scale is presented in Fig. 10 for varying cold boundary temperatures. The ordinate of Fig. 10 represents the normalized representative velocity vector ($\vec{\mathbf{v}}_{rn}$) defined by Eq. (24), and the abscissa represents

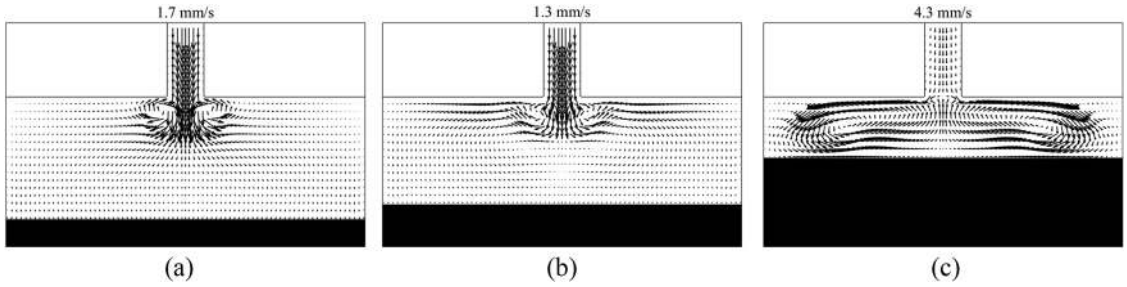

FIG. 9. Solidification phenomenon for Cu at (a) 10 s, (b) 24 s, and (c) 100 s.

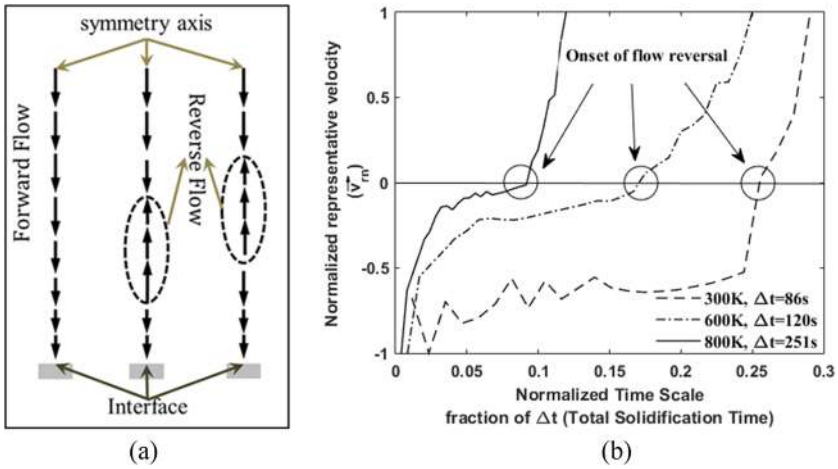

FIG. 10. (a) Schematic representation of the velocity vectors along the central symmetry line for forward and reverse flow. (b) Onset of flow reversal for varying cold boundary temperatures T_b on the normalized time scale.

the normalized solidification time scale. In this plot, the normalized time instant at which the sign of $\vec{\mathbf{v}}_{rn}$ changes from $-ve$ to $+ve$ designates the onset of flow reversal. As is evident from Fig. 10, the faster cooling rate associated with the colder bottom surface temperature delays the flow reversal phenomena. For instance, a cold boundary temperature of 800 K causes more than 90% of the total solidification time to be dominated by the reverse flow pattern, while with T_b = 300 K, the reverse flow pattern is encountered during the last 75% of the total solidification duration.

3. Effect of varying initial conditions

For the bottom cooled configuration, the buoyancy force opposes the shrinkage induced flow. Since the local buoyancy source term depends on $\Delta T = T - T_{ref}$, the initial temperature of the liquid melt is expected to play a key role in defining the evolution of this source term. With the flow reversal phenomena being identified as a direct consequence of the opposing buoyancy source term, we intend to study the effect of varying initial temperatures on the onset of flow reversal. Three different initial temperatures of the Al melt (T_i = 1073 K, 1223 K, and 1373 K with an increment of 150 K) are considered. The cold boundary temperature (T_b) is maintained at a fixed value of 800 K, and the cavity–riser size and shape is kept unaltered. Figures 11(a)–11(c) show the snapshots of the velocity profile in the cavity during the onset of flow reversal for different initial conditions, respectively. The higher the initial temperature of the melt, the slower the solidification rate. An analysis akin to the one with varying cold boundary (T_b) conditions and presented in Fig. 10 on the onset of flow reversal with respect to the normalized time scale is carried out for varying initial temperatures (T_i). Figure 11(d) shows the onset of flow reversal on a normalized time scale vs $\vec{\mathbf{v}}_{rn}$ plot. Once again in Fig. 11(d), the sign change of $\vec{\mathbf{v}}_{rn}$ from $-ve$ to $+ve$ designates the onset of flow reversal in the normalized time scale framework for the corresponding initial temperatures. As is evident from Fig. 11(d), higher initial temperature promotes relatively faster attainment of flow reversal in the normalized time scale representation.

4. Effect of varying cavity height

The parametric study is concluded with the effect of cavity height on the onset of flow reversal during the directional solidification of pure Al in a bottom cooled cavity. In the bottom cooled configuration, the thickness of the stably stratified melt (higher density of the melt at the bottom and lower density at top) increases with an increase in cavity height. As a result, the shrinkage induced downward movement of the melt from the riser along the center line of the cavity is expected to encounter more resistance for the increased cavity height. For this analysis, the constant temperature boundary condition (T_b) and initial temperature of the the melt (T_i) are kept at

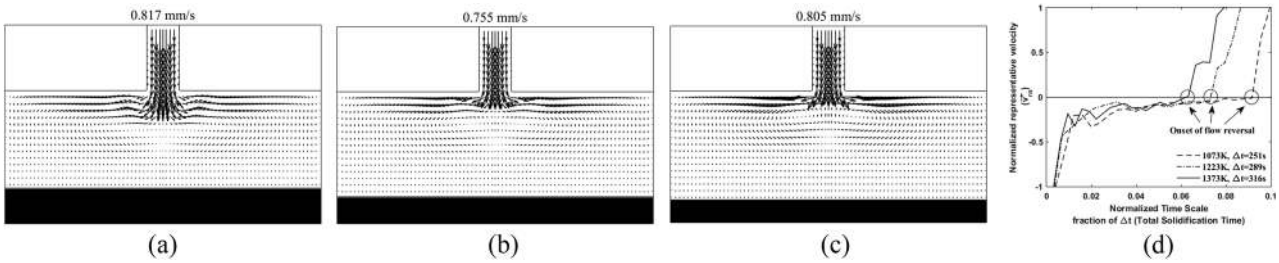

FIG. 11. Onset of flow reversal for varying initial conditions (a) T_i = 1073 K, (b) T_i = 1223 K, and (c) T_i = 1373 K; and (d) mapping of flow reversal for varying initial conditions on the normalized time scale.

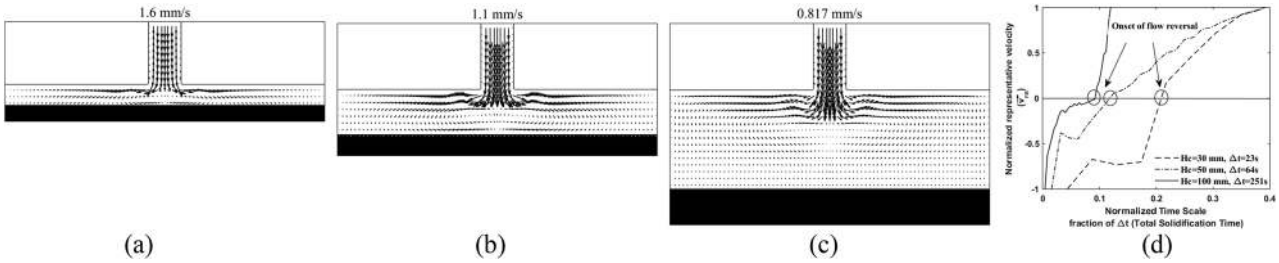

FIG. 12. Onset of flow reversal for varying cavity heights: (a) H_C = 30 mm, (b) H_C = 50 mm, and (c) H_C = 100 mm, and (d) mapping of flow reversal for varying casting heights on the normalized time scale.

FIG. 13. Solid–liquid interface deformation in the form of a plunge pool adjacent to the riser opening to the cavity for (a) H_c = 30 mm and (b) H_c = 50 mm.

fixed values of 800 K and 1073 K, respectively, while the cavity height is varied. Three different cavity heights H_c = 30 mm, H_c = 50 mm, and H_c = 100 mm are considered for this analysis. Figures 12(a)–12(c) show the snapshots of the velocity profile in the cavity during the onset of flow reversal for different cavity heights, respectively. The larger the cavity height, the greater the resistance to the shrinkage induced flow. A similar analysis to those with varying T_b and T_i on the onset of flow reversal in a normalized time scale framework is carried out for varying cavity height (H_c). Figure 12(d) shows the onset of flow reversal on a normalized time scale vs $\bar{\mathbf{v}}_{rn}$ plot. Once again in Fig. 12(d), the sign change of $\bar{\mathbf{v}}_{rn}$ from $-ve$ to $+ve$ represents the onset of flow reversal in the normalized time scale framework for corresponding cavity heights. As is evident from Fig. 12(d), a larger cavity height causes an early flow reversal.

Finally, deformation of otherwise planar interface growth due to the shrinkage induced flow is presented in Fig. 13 for two different cavity heights, viz., 30 mm and 50 mm. The bottom boundary condition and the initial temperature of the Al melt are considered to be T_b = 800 K and T_i = 1073 K, respectively. Figures 13(a) and 13(b) clearly show the formation of a plunge-pool adjacent to the location of the riser opening to the cavity. Although this deformation of the planar front is marginal for pure Al, we might expect it to be more significant during alloy solidification, leading to interesting compositional segregation.

VI. CONCLUSIONS

A numerical model is proposed for predicting the shrinkage induced flow during directional solidification of pure and amorphous materials in a bottom cooled cavity. The shrinkage induced flow is found to be opposed by the buoyancy effect, leading to a distinct flow reversal phenomenon. The most important achievements and outcomes associated with this study are as follows:

1. The system of governing equations are considered and modified to incorporate the shrinkage effect by implementing the volume averaging method.
2. A novel volume fraction updating method is proposed to track the distinct interface during solidification of the pure material.
3. For the bottom cooled configuration, the buoyancy source term is found to play a significant role in defining the convection pattern. The shrinkage induced flow is opposed by the otherwise stably stratified density gradient, leading to a distinct flow reversal phenomenon during the directional solidification in the bottom cooled configuration.
4. For low Prandtl number materials such as aluminum and copper, deformation of isotherms adjacent to the undulated solid–liquid interface causes the buoyancy force aided with shrinkage induced inertia to lift the fluid vertically upward along the symmetric center line of the cavity, leading to the sustenance of the flow reversal. Flow reversal does not occur until the central depression of the solid–liquid interface is evolved. On the other hand, for high Prandtl substances such as coconut oil, perturbation of the thermal field due to the shrinkage induced flow field is easily attained. As a result, an early onset of flow reversal can be observed, almost coinciding with the very inception of solid front growth.
5. The major outcome of the proposed model in terms of flow reversal phenomena is experimentally validated, considering the directional solidification of coconut oil in a bottom cooled cavity. The experimentally measured flow field and liquid–mushy interface locations are compared with 3D numerical predictions in reasonable agreements.
6. 2D numerical studies are performed for the directional solidification of two different pure metals, namely, Al and Cu. Both case studies revealed the onset and sustenance of flow reversal during the solidification process.

7. The effect of varying cold boundary temperature, initial temperature of the melt, and cavity height on the onset of flow reversal is studied for bottom cooled directional solidification of pure Al. An increase in all these three parameters is found to promote an early flow reversal when time scale is normalized with respect to the total solidification time.
8. The shrinkage induced flow field is found to cause deformation of the planar solid front in the form of a plunge pool. For the square riser, the shape of the plunge pool is found to have a distinct orientation along the length and width of the cavity.

The present analysis will be of great relevance toward the modeling of macro-scale shrinkage defects and prediction of composition heterogeneity during directional alloy solidification.

ACKNOWLEDGMENTS

The authors gratefully acknowledge the financial support received from the Department of Science and Technology (DST), India (Grant No. DST/TMD/MES/2K17/44), and the Seed Grant (Grant No. I/SEED/PRC/20150023) at IIT Jodhpur. The partial support from another DST project (Grant No. EMR/2015/001140) for the development of the MicroVec PIV system at IIT Bombay is acknowledged. The authors would also like to acknowledge the role of the Grammarly App during the preparation of this manuscript.

REFERENCES

[1]P. Dutta, Y. Joshi, and R. Janaswamy, "Thermal modeling of gas tungsten arc welding process with nonaxisymmetric boundary conditions," Numer. Heat Transfer, Part A **27**, 499–518 (1995).
[2]S. Sarkar, P. M. Raj, S. Chakraborty, and P. Dutta, "Three-dimensional computational modeling of momentum, heat, and mass transfer in a laser surface alloying process," Numer. Heat Transfer, Part A **42**, 307–326 (2002).
[3]P. M. Raj, S. Sarkar, S. Chakraborty, G. Phanikumar, P. Dutta, and K. Chattopadhyay, "Modelling of transport phenomena in laser surface alloying with distributed species mass source," Int. J. Heat Fluid Flow **23**, 298–307 (2002).
[4]D. Kashchiev, "Determining the curvature dependence of surface tension," J. Chem. Phys. **118**, 9081–9083 (2003).
[5]Y. Zhang and A. Faghri, "Melting of a subcooled mixed powder bed with constant heat flux heating," Int. J. Heat Mass Transfer **42**, 775–788 (1999).
[6]T. Chen and Y. Zhang, "Three-dimensional modeling of selective laser sintering of two-component metal powder layers," J. Manuf. Sci. Eng. **128**, 299 (2006).
[7]B. Xiao and Y. Zhang, "Partial melting and resolidification of metal powder in selective laser sintering," J. Thermophys. Heat Transfer **20**, 439–448 (2006).
[8]S. O. Unverdi and G. Tryggvason, "A front-tracking method for viscous, incompressible, multi-fluid flows," J. Comput. Phys. **100**, 25–37 (1992).
[9]G. Tryggvason, B. Bunner, A. Esmaeeli, D. Juric, N. Al-Rawahi, W. Tauber, J. Han, S. Nas, and Y.-J. Jan, "A front-tracking method for the computations of multiphase flow," J. Comput. Phys. **169**, 708–759 (2001).
[10]F. S. De Sousa, N. Mangiavacchi, L. G. Nonato, A. Castelo, M. F. Tomé, V. G. Ferreira, J. A. Cuminato, and S. McKee, "A front-tracking/front-capturing method for the simulation of 3D multi-fluid flows with free surfaces," J. Comput. Phys. **198**, 469–499 (2004).
[11]M. Sussman, E. Fatemi, P. Smereka, and S. Osher, "An improved level set method for incompressible two-phase flows," Comput. Fluids **27**, 663–680 (1998).
[12]F. H. Harlow and J. E. Welch, "Numerical calculation of time-dependent viscous incompressible flow of fluid with free surface," Phys. Fluids **8**, 2182–2189 (1965).
[13]V. R. Voller, C. R. Swaminathan, and B. G. Thomas, "Fixed grid techniques for phase change problems: A review," Int. J. Numer. Methods Eng. **30**, 875–898 (1990).
[14]V. R. Voller, M. Cross, and N. C. Markatos, "An enthalpy method for convection/diffusion phase change," Int. J. Numer. Methods Eng. **24**, 271–284 (1987).
[15]V. R. Voller and C. Prakash, "A fixed grid numerical modelling methodology for convection-diffusion mushy region phase-change problems," Int. J. Heat Mass Transfer **30**, 1709–1719 (1987).
[16]A. D. Brent, V. R. Voller, and K. J. Reid, "Enthalpy-porosity technique for modeling convection-diffusion phase change: Application to the melting of a pure metal," Numer. Heat Transfer Part A **13**, 297–318 (1988).
[17]C. R. Swaminathan and V. R. Voller, "A general enthalpy method for modeling solidification processes," Metall. Trans. B **23**, 651–664 (1992).
[18]C. R. Swaminathan and V. R. Voller, "On the enthalpy method," Int. J. Numer. Methods Heat Fluid Flow **3**, 233–244 (1993).
[19]P. R. Chakraborty, "Enthalpy porosity model for melting and solidification of pure-substances with large difference in phase specific heats," Int. Commun. Heat Mass Transfer **81**, 183–189 (2017).
[20]D. Xu and Q. Li, "Gravity- and solidification-shrinkage-induced liquid flow in a horizontally solidified alloy ingot," Numer. Heat Transfer **20**, 203–221 (1991).
[21]K. C. Chiang and H. L. Tsai, "Shrinkage-induced fluid flow and domain change in two-dimensional alloy solidification," Int. J. Heat Mass Transfer **35**, 1763–1770 (1992).
[22]K. C. Chiang and H. L. Tsai, "Interaction between shrinkage-induced fluid flow and natural convection during alloy solidification," Int. J. Heat Mass Transfer **35**, 1771–1778 (1992).
[23]M. J. M. Krane and F. P. Incropera, "Analysis of the effect of shrinkage on macrosegregation in alloy solidification," Metall. Mater. Trans. A **26**, 2329–2339 (1995).
[24]G. Kefayati, "Lattice Boltzmann simulation of double-diffusive natural convection of viscoplastic fluids in a porous cavity," Phys. Fluids **31**, 013105 (2019).
[25]O. Satbhai, S. Roy, S. Ghosh, S. Chakraborty, and R. Lakkaraju, "Comparison of the quasi-steady-state heat transport in phase-change and classical Rayleigh–Bénard convection for a wide range of Stefan number and Rayleigh number," Phys. Fluids **31**, 096605 (2019).
[26]M. C. Flemings, "Solidification processing," Metall. Trans. **5**, 2121–2134 (1974).
[27]H. Kato and J. R. Cahoon, "Inverse segregation in directionally solidified Al-Cu-Ti alloys with equiaxed grains," Metall. Trans. A **16**, 579–587 (1985).
[28]R. S. Rerko, C. Beckermann *et al.*, "Effect of melt convection and solid transport on macrosegregation and grain structure in equiaxed Al–Cu alloys," Mater. Sci. Eng.: A **347**, 186–197 (2003).
[29]I. L. Beckermann, C. A. Santos, A. Garcia, and V. R. Voller, "Analytical, numerical, and experimental analysis of inverse macrosegregation during upward unidirectional solidification of Al–Cu alloys," Metall. Mater. Trans. B **35**, 285–297 (2004).
[30]I. L. Ferreira, J. E. Spinelli, and A. Garcia, "Gravity-driven inverse segregation during transient upward directional solidification of Sn–Pb hypoeutectic alloys," J. Alloys Compds. **475**, 396–400 (2009).
[31]I. Ziv and F. Weinberg, "The columnar-to-equiaxed transition in Al_3 Pct Cu," Metall. Trans. B **20**, 731–734 (1989).
[32]J. Alkemper, S. Sous, C. Stöcker, and L. Ratke, "Directional solidification in an aerogel furnace with high resolution optical temperature measurements," J. Cryst. Growth **191**, 252–260 (1998).
[33]C.-A. Gandin, "Experimental study of the transition from constrained to unconstrained growth during directional solidification," ISIJ Int. **40**, 971–979 (2000).
[34]V. Kumar, M. Kumawat, A. Srivastava, and S. Karagadde, "Mechanism of flow reversal during solidification of an anomalous liquid," Phys. Fluids **29**, 123603 (2017).
[35]V. Kumar, A. Srivastava, and S. Karagadde, "Real-time observations of density anomaly driven convection and front instability during solidification of water," J. Heat Transfer **140**, 042503 (2018).

[36]V. Kumar, A. Srivastava, and S. Karagadde, "Generalized regimes for the formation of stratified regions during freezing of multi-component mixtures," Phys. Fluids **31**, 123602 (2019).
[37]H. K. Versteeg and W. Malalasekera, *An Introduction to Computational Fluid Dynamics: The Finite Volume Method* (Pearson Education, 2007).
[38]W. D. Bennon and F. P. Incropera, "A continuum model for momentum, heat and species transport in binary solid-liquid phase change systems—I. Model formulation," Int. J. Heat Mass Transfer **30**, 2161–2170 (1987).
[39]W. D. Bennon and F. P. Incropera, "A continuum model for momentum, heat and species transport in binary solid-liquid phase change systems—II. Application to solidification in a rectangular cavity," Int. J. Heat Mass Transfer **30**, 2171–2187 (1987).
[40]S. Patankar, *Numerical Heat Transfer and Fluid Flow* (CRC Press, 1980).
[41]P. K. Stansby, "Solitary wave run up and overtopping by a semi-implicit finite-volume shallow-water boussinesq model," J. Hydraul. Res. **41**, 639–647 (2003).
[42]Fluent ANSYS, *18.1, Theory Guide, Ansys* (Ansys, Inc., 2017).
[43]Fluent ANSYS, *18.1, User Guide, Ansys* (Ansys, Inc., 2017).
[44]V. Kumar, A. Srivastava, and S. Karagadde, "Do the intrusive probes alter the characteristic length-scales of natural convection?," J. Flow Visualization Image Process. **25**, 207 (2018).
[45]V. Kumar, A. Srivastava, and S. Karagadde, "Compositional dependency of double-diffusive layers during binary alloy solidification: Full-field measurements and quantification," Phys. Fluids **30**, 113603 (2018).
[46]C.-A. Gandin, "From constrained to unconstrained growth during directional solidification," Acta Mater. **48**, 2483–2501 (2000).
[47]A. T. Dinsdale and P. N. Quested, "The viscosity of aluminium and its alloys—A review of data and models," J. Mater. Sci. **39**, 7221–7228 (2004).
[48]S. Motakef, "Magnetic field elimination of convective interference with segregation during vertical-Bridgman growth of doped semiconductors," J. Cryst. Growth **104**, 833–850 (1990).
[49]R. E. Timms, "Physical properties of oils and mixtures of oils," J. Am. Oil Chem. Soc. **62**, 241–249 (1985).
[50]M. J. Assael, A. E. Kalyva, K. D. Antoniadis, R. Michael Banish, I. Egry, J. Wu, E. Kaschnitz, and W. A. Wakeham, "Reference data for the density and viscosity of liquid copper and liquid tin," J. Phys. Chem. Ref. Data **39**, 033105 (2010).
[51]J. A. Cahill and A. D. Kirshenbaum, "The density of liquid copper from its melting point (1356°K.) to 2500°K. and an estimate of its critical constants," J. Phys. Chem. **66**, 1080–1082 (1962).